

# Gamma-Ray Polarimetry of the Crab Pulsar Observed by POLAR

Han-Cheng Li<sup>1,2,3</sup>\*, Nicolas Produit<sup>1</sup>, Shuang-Nan Zhang<sup>2,3</sup>, Merlin Kole<sup>4</sup>, Jian-Chao Sun<sup>2,3</sup>, Ming-Yu Ge<sup>2,3</sup>, Nicolas De Angelis<sup>4</sup>, Johannes Hulsman<sup>4</sup>, Zheng-Heng Li<sup>5</sup>, Li-Ming Song<sup>2,3</sup>, Teresa Tymieniecka<sup>6</sup>, Bo-Bing Wu<sup>2</sup>, Xin Wu<sup>4</sup>, Yuan-Hao Wang<sup>2</sup>, Shao-Lin Xiong<sup>2</sup>, Yong-Jie Zhang<sup>2</sup>, Yi Zhao<sup>2,7</sup>, and Shi-Jie Zheng<sup>2</sup>

<sup>1</sup>Department of Astronomy, University of Geneva, 16 Chemin d'Ecogia, 1290 Versoix, Switzerland

<sup>2</sup>Key Laboratory of Particle Astrophysics, Institute of High Energy Physics, Chinese Academy of Sciences, Beijing 100049, China

<sup>3</sup>University of Chinese Academy of Sciences, Beijing 100049, China

<sup>4</sup>Department of Nuclear and Particle Physics, University of Geneva, 24 Quai Ernest-Ansermet, 1205 Geneva, Switzerland

<sup>5</sup>Center for Transformative Science, ShanghaiTech University, Shanghai 201210, China

<sup>6</sup>National Centre for Nuclear Research, ul. A. Soltana 7, 05-400 Otwock, Swierk, Poland

<sup>7</sup>Department of Astronomy, Beijing Normal University, Beijing 100875, China

22 February 2022

## ABSTRACT

The X/γ ray polarimetry of the Crab pulsar/nebula is believed to hold crucial information on their emission models. In the past, several missions have shown evidence of polarized emission from the Crab. The significance of these measurements remains however limited. New measurements are therefore required. POLAR is a wide Field of View Compton-scattering polarimeter (sensitive in 50–500 keV) onboard the Chinese spacelab Tiangong-2 which took data from September 2016 to April 2017. Although not designed to perform polarization measurements of pulsars, we present here a novel method which can be applied to POLAR as well as that of other wide Field of View polarimeters. The novel polarimetric joint-fitting method for the Crab pulsar observations with POLAR, allows us to obtain constraining measurements of the pulsar component. The best fitted values and corresponding 1σ deviations for the averaged phase interval: (PD=14<sup>+15</sup><sub>-10</sub>%, PA=108<sup>+33</sup><sub>-54</sub>°), for Peak 1: (PD=17<sup>+18</sup><sub>-12</sub>%, PA=174<sup>+39</sup><sub>-36</sub>°) and for Peak 2: (PD=16<sup>+16</sup><sub>-11</sub>%, PA=78<sup>+39</sup><sub>-30</sub>°). Further more, the 3σ upper limits on the polarization degree are for the averaged phase interval (55%), Peak 1 (66%) and Peak 2 (57%). Finally, to illustrate the capabilities of this method in the future, we simulated two years observation to the Crab pulsar with POLAR-2. The results show that POLAR-2 is able to confirm the emission to be polarized with 5σ and 4σ confidence level if the Crab pulsar is polarized at 20% and 10% respectively.

**Key words:** Instrumentation: polarimeters – Methods: data analysis – Stars: pulsars: individual – Techniques: polarimetric – Gamma rays: general

## 1 INTRODUCTION

The Crab pulsar (PSR B0531+21) is located in the heart of the Crab nebula (supernova remnant of SN 1054). As an isolated pulsar, the Crab pulsar is rotation-powered with  $\dot{E} \approx 5 \times 10^{38}$  erg/s. Electromagnetic radiation is emitted from its co-rotating strong dipole magnetic field. The Crab pulsar shows a double-pulse structure over all wavelengths, with pulse phase intervals defined as Peak 1 (P1), Peak 2 (P2), and the Off Pulse (OP) where the nebula dominates. The broadband high brightness makes it widely studied over the past five decades by monitoring its spectral, timing and imaging properties. Thereby multiple emission models have been developed, including polar gap model (Ruderman & Sutherland 1975), outer gap model (Cheng et al. 1986a,b), slot gap model (Hirotani 2008) and annular gap model (Du et al. 2010), etc. Despite all these efforts, detailed physical questions related to the emission mechanism and region, geometry of source, etc., are yet to be precisely understood. Polarimetry is widely be-

lieved to be a unique probe to answer some of these questions; phase resolved polarimetry is more crucial since the observed emission regions are phase-dependent. Some theoretical predictions have been made by Takata et al. (2007); Pétri (2013); Harding & Kalapotharakos (2017). The two parameters of polarimetry are commonly referred as Polarization Degree (PD) and Polarization Angle (PA). Although the actual polarization of sources can be a mixture of linear and circular components, the measurements of current X/γ ray polarimeters are limited to the linear polarization only. Therefore, in this and all cited works here, we only refer to the linear polarization.

The OSO-8 mission with Bragg crystal polarimeters performed the first successful astrophysical polarization measurements in the X-ray energy band. These measurements were of the Crab nebula at energies of 2.6 keV and 5.2 keV (Weisskopf et al. 1976, 1978). At 2.6 keV the results are (PD=15.7±1.5%, PA=161.1±2.8°) for Averaged Phase interval of the Crab (AP, including pulsar and nebula), (PD=19.2±1.0%, PA=156.4±1.4°) for OP (only nebula), and similar results were found at ~ 5.2 keV. These results support the theory that synchrotron radiation is responsible for the

\* Contact e-mail: [hancheng.li@unige.ch](mailto:hancheng.li@unige.ch)

X-ray emission from the Crab nebula. Long after that, the SPI and IBIS on board the INTEGRAL mission measured the hard X-ray polarization measurements for the Crab nebula and pulsar by accumulating Compton-scattering events. The main results can be summarized as Forot et al. (2008) (200-800 keV): AP (PD= $47^{+19}_{-13}\%$ , PA= $100\pm 11^\circ$ ), P1+P2 (PD= $42^{+30}_{-16}\%$ , PA= $70\pm 20^\circ$ ), OP (PD> $>72\%$ , PA= $120.6\pm 8.5^\circ$ ); Dean et al. (2008) (100-1000 keV): OP (PD= $47\pm 10\%$ , PA= $123\pm 11^\circ$ ); Chauvin et al. (2013) (130-400 keV): AP (PD= $28\pm 6\%$ , PA= $117\pm 9^\circ$ ); Jourdain & Roques (2019) (130-400 keV): AP (PD= $24\pm 4\%$ , PA= $120\pm 6^\circ$ ). However, the first two publications indicated a high PD for the Crab, whereas the latter two obtained much lower PD measurements. Additionally, as neither of the two INTEGRAL instruments is a dedicated polarimeter, no on-ground calibration was performed. As a result, one cannot validate the analysis and the magnitude of the systematic uncertainty on the measurements.

The polarization parameters of the Crab pulsar and nebula have been precisely measured at optical wavelengths. The latest optical polarization measurements on the Crab pulsar and nebula were done by OPTIMA (610 and 1400 MHz) (Słowikowska et al. 2009) and HST (Moran et al. 2013). For the Crab pulsar: 1) OPTIMA measured for the AP (PD= $5.5\pm 0.1\%$ , PA= $96.4\pm 0.1^\circ$ ), and the phase-resolved results show that PDs are higher in the bridge and off-pulse region than those in the two peaks, and the PAs swing through a large angle in both peaks; 2) HST measured for the AP (PD= $5.2\pm 0.3\%$ , PA= $105.1\pm 1.6^\circ$ ). For the Crab nebula: OPTIMA measured (PD= $9.7\pm 0.1\%$ , PA= $139.8\pm 0.2^\circ$ ) when the region is near the pulsar; the averaged PA value is  $140^\circ$  in the region 2-3 arcsec away from the pulsar; beyond 5 arcsec the PA exceeds  $155^\circ$  and becomes highly position dependent.

In recent years, several dedicated Compton-scattering or Photoelectron-track polarimeters have obtained more precise polarization measurements in X/ $\gamma$  ray bands (Chattopadhyay 2021). For example, PoGO+ (Compton, 20-160 keV, Chauvin et al. (2017)) measured polarization for AP (PD= $20.9\pm 5.0\%$ , PA= $131.3\pm 6.8^\circ$ ), P1 (PD= $0^{+29}_{-0}\%$ , PA= $153\pm 43^\circ$ ), P2 (PD= $33.5^{+18.6}_{-22.3}\%$ , PA= $153\pm 43^\circ$ ) and OP (PD= $17.4^{+8.6}_{-9.3}\%$ , PA= $137\pm 15^\circ$ ). Their results also rejected a high PD. AstroSat CZTI (Compton, 100-380 keV, Vadawale et al. (2018)) measured polarization for AP (PD= $32.7\pm 5.8\%$ , PA= $143.5\pm 2.8^\circ$ ) and OP ( $39.0\pm 10.0\%$ ,  $140.9\pm 3.7^\circ$ ). Based on further phase-resolved results, they claimed that there are variable polarization properties within the off-pulse region and a swing of the polarization angle across the pulse peaks. Hitomi SGD (Compton, 60-160 keV, Hitomi Collaboration et al. (2018)) also obtained a significant polarization measurement for AP of (PD= $22.1\pm 10.6\%$ , PA= $110.7^{+13.2}_{-13.0}$ ) with 5 ks short exposure time. More recently, a collimated Cube-Sate PolarLight (Photoelectron, 3.0–4.5 keV, Feng et al. (2020)) measured polarization for AP (PD= $15.3^{+3.1}_{-3.0}\%$ , PA= $145.8\pm 5.7^\circ$ ), P1+P2 (PD= $15.8\pm 3.9\%$ , PA= $147.6\pm 7.0^\circ$ ), OP (PD= $14.0^{+5.2}_{-5.4}\%$ , PA= $142.4\pm 11.0^\circ$ ). They further performed time-dependent polarization analysis, and found that PD decreased after the glitch of the Crab pulsar on 23 July 2019. The polarization results in X/ $\gamma$  ray bands mentioned above are listed in Table D2.

POLAR is a dedicated Gamma-Ray Burst (GRB) Compton-scattering polarimeter sensitive in 50-500 keV energy range (Produit et al. 2005, 2018). POLAR was launched on September 2016 on-board the second Chinese space laboratory Tiangong-2 (TG-2). The zenith of POLAR was continuously pointing to the sky, and it was working in a scanning observation mode while running it during its orbit. Given the random occurrence of GRBs in the sky, POLAR is equipped with a wide Field of View (FoV) ( $\sim 2\pi$  Sr) and a large

effective area ( $400\text{ cm}^2$  at 300 keV). These features make it one of the most sensitive instruments for GRB detections in its energy range. During its six-month observation, POLAR detected 55 GRBs (Xiong et al. 2017). In order to estimate systematic effects, POLAR has been carefully calibrated both on-ground and in-orbit (Kole et al. 2017; Li et al. 2018) for polarization and spectral responses. Thereafter, 14 of the detected GRBs have been used to preform polarization analyses (Zhang et al. 2019a; Burgess et al. 2019; Kole et al. 2020).

Apart from transients, such as GRBs, POLAR cannot observe persistent celestial sources due to their low Signal to Noise Ratio (SNR) resulted from POLAR's large FoV. However, POLAR can monitor some luminous X-ray pulsars. The periodic nature of pulsars makes it possible to stack the signal by aligning pulse phase values. Thanks to the well established timing analysis for pulsars, the pulse phase parameter can be derived. Based on the pulse phase parameter, spectrum and modulation curves can be additionally extracted for further studies. POLAR has detected folded pulsations from both the Crab pulsar and the PSR B1509-58 significantly (detailed analyses on observation and simulation verification can be found in Li et al. (2017); Li & POLAR Collaboration (2021)). Since POLAR is not dedicated for pulsar studies, the SNR of pulsar detection is much lower than that of GRBs, but this can partially be compensated using the larger exposure time for pulsars. Limited by the low SNR in the end, PSR B1509-58 has not yet been further studied. While the Crab pulsar detection was much more significant, and was firstly chosen to test pulsar navigation algorithm to predict the TG-2 orbital parameters (Zheng et al. 2017). As POLAR is a non-pointing wide FoV instrument, the observation datasets are complicated by multiple observational parameters like incoming photon angles. Therefore, before proceeding with the polarization studies of the Crab pulsar using POLAR data, we performed a phase-resolved spectroscopy for checking the spectral responses from all incoming angles (Li et al. 2019). Previous timing and spectral studies of the Crab pulsar with POLAR data served as timing and spectral calibrations to the POLAR instrument, and lay the groundwork for the polarization study.

In this paper, we present the polarimetric methodology developed as well as the resulting polarization measurements of the Crab pulsar with POLAR. In Section 2 we introduce the observations and data selection criteria. The methodology of the polarimetry of the Crab pulsar is described in Section 3. In Section 4, phase-resolved polarization results are presented. Subsequently, in Section 5, we show the future mission POLAR-2's prospective polarimetry on the Crab pulsar. Finally, we draw the main conclusions of this paper in Section 6.

## 2 OBSERVATION

POLAR took approximately six months in-orbit observation data from September 2016 to April 2017, during which the Crab pulsar was visible to POLAR when it passed through POLAR's FoV. The timing analysis used here for the Crab pulsar is based on previous work (Li et al. 2017, 2019; Li & POLAR Collaboration 2021). Note that phase zero reference in our analysis is taken from the X-ray observation. The general data pipeline is based on the standard method described in (Li et al. 2018). This pipeline handles processes such as baseline/noise subtraction, signal crosstalk correction, energy reconstruction, as well as filtering of cosmic-ray events and post-cosmic-ray events. Additionally, the Good Time Interval (GTI) were generated by applying a count rate threshold on the one-second-binning light curves. With GTI we mainly excluded high background intervals caused by the South Atlantic Anomaly (SAA), the high lat-

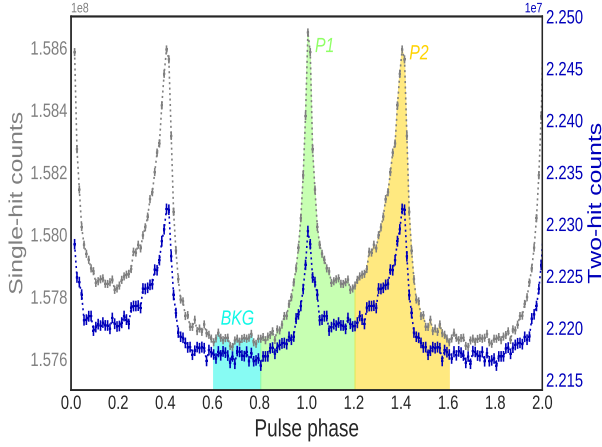


**Figure 1. Pulse profiles of single-hit and two-hit events.** The definitions of different phase intervals in this work are defined as: OP (0.6-0.8), P1 (0-0.2 || 0.8-1.0), P2 (0.2-0.6). OP contains the nebula and background photons that cannot be distinguished by POLAR, so the whole OP is treated as background (BKG). The colored regions on the pulse profiles display the different phase intervals (shifted 1 phase to make it clear). Note that only two-hit events (which contain Compton-scattering events) are used for the polarization analysis.

itude areas, GRBs, solar flares, etc. With GTI selection we obtain a total of  $\sim 4400$  ks exposure time to the Crab pulsar.

Using this selection the pulse profile can be folded versus different observational parameters. Figure 1 shows the pulse profiles of the so-called single-hit events and two-hit events. The two-hit events contain at least two channels within POLAR above the trigger threshold while the single-hit events only contain one triggered channel. This distinction is important as only two-hit events can be used for polarization studies while the single-hit events can only be used for timing and spectral analysis such as in (Li et al. 2019). The two profiles are precisely aligned, but two-hit counts are  $\sim 14\%$  of the single-hit counts. The definitions of the different phase intervals in this work are: P1 (0-0.2 || 0.8-1.0), P2 (0.2-0.6) and OP (0.6-0.8). As a wide FoV detector, POLAR cannot distinguish pulsar, nebula and background (signal from neither pulsar nor nebula) components spatially, so the pulse phase is the only parameter that can be used for dividing these components. We assume that the nebula and background are phase independent, and that the pulsar has no contribution in the OP interval. In this case, the OP interval contains only the nebula and background components, which can be subtracted from P1 and P2 intervals to get pure pulsar emissions. To summarize, we cannot extract the nebula component from the background, so that both of them are subtracted from the on-pulse intervals. Therefore, the polarization measurements in this work are only for pulsar emissions without the nebula contribution.

Before investigating other observational parameters, we have to introduce three different coordinate systems used in this work as shown in Figure 2, which are: 1) POLAR coordinates, the local coordinates of POLAR detector, the incoming angle of a source can be described as  $\theta$  (zenith angle) and  $\phi$  (azimuthal angle); we note that the definitions of  $\theta$  and  $\phi$  here are different from the ones in Figure 7; 2) source coordinates, its Z-axis points from the detector to the source (inverse to the source's incident direction), and the  $X'$ - $Y'$  plane is perpendicular to the source's incident direction; 3) J2000/Equatorial coordinates, the North-East plane of which is commonly used to define the PA value (from the North to the East) and to demonstrate the polarization vector. First, unlike the GRB observation, which

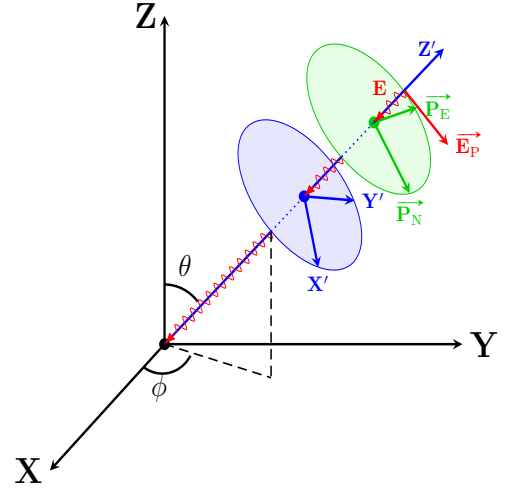


**Figure 2. Coordinate definitions in this work.** The POLAR coordinate system (in black) is the local coordinate system for the POLAR detector, when photons (in energy  $E$ ) of a source arrive at POLAR, the incident angle of them can be described as  $\theta$  (angle from POLAR's zenith angle) and  $\phi$  (azimuthal angle). The source coordinate (in blue) is rotated from the POLAR coordinate by  $\theta$  and  $\phi$ , its Z-axis points from the detector to the source (inverse to the source's incident direction), and the  $X'$ - $Y'$  plane is perpendicular to the source's incident direction. The J2000/Equatorial coordinate (in green) is the standard source location coordinate system, the North-East (projections onto the source plane are  $\mathbf{P}_N$ - $\mathbf{P}_E$ ) plane is used to define the PA value (from the North to the East) and to demonstrate the polarization vector  $\mathbf{E}_P$ . Detailed projection illustration is shown in Figure 5.

happens within a short duration where the incident angle of the source in the POLAR local coordinate does not change significantly, the Crab pulsar observation angle relative to the detector varies over the entire mission so that data with multiple incident angles need to be separated. In the previous work of Li et al. (2017), the pulse profile versus the incoming angle  $\theta$  shows that the Crab pulsar is visible to POLAR when  $\theta$  is below  $\sim 102^\circ$ . In order to resolve this parameter, we employed HealPix (HP, Górski et al. (2005)) to divide POLAR's local sky into 768 HP bins (numbering is 0-767), where  $N_{\text{side}} = 8$  and RING numbering schedule is used. Given the conditional visibility, the first 400 HP bins (0-399) are considered, more details can be found in (Li et al. 2019).

We accumulate the data into each HP bins. The pulse profiles of two-hit events as a function of HP bins are shown in Figure 3, where one can observe how the statistics over HP bins differ from each other. In order to select a sub-sample of HP, we calculated the pulse significance of the Crab two-hit events for 400 HP bins by using equation (17) of Li & Ma (1983). Figure 4 shows the pulse significance as a function of HP. For the polarization analysis, we set a threshold value of  $2\sigma$  on pulse significance (red dashed line in Figure 4). Additionally, we cut data with incident angle  $\theta > 70^\circ$  (i.e., HP > 239), since the large off-axis incidence has worse polarization response as explained in Appendix B. Finally, a sub-sample of 108 HP datasets for the Crab pulsar is used. These are listed in Table D1, and the total exposure time of the subsample is  $\sim 1710$  ks.

Furthermore, for the Crab pulsar observation within one specific HP bin, the North-East plane of the J2000 coordinates onto the  $X'$ - $Y'$  plane of the source coordinates also change. In other words, the source rotates along the incident direction even when the local incident angles are fixed. Figure 5 shows the  $X'$ - $Y'$  plane of the

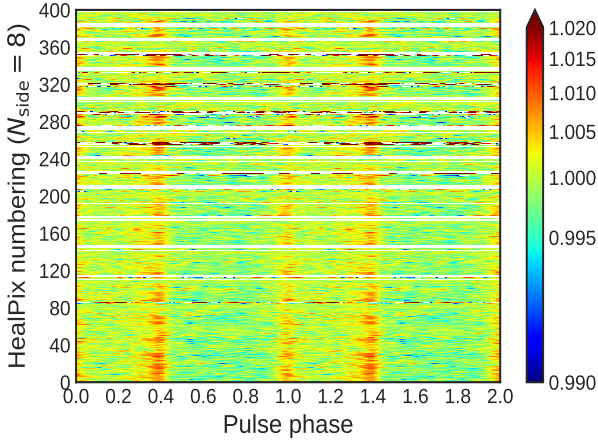


**Figure 3.** Pulse profiles of two-hit events v.s. the healpix bin (HP). The z-axis contains the normalized counts of the pulse profile of each HP bin. The statistics of signal vary with the HP bins since the exposure time and sensitivity of each HP bin is different.

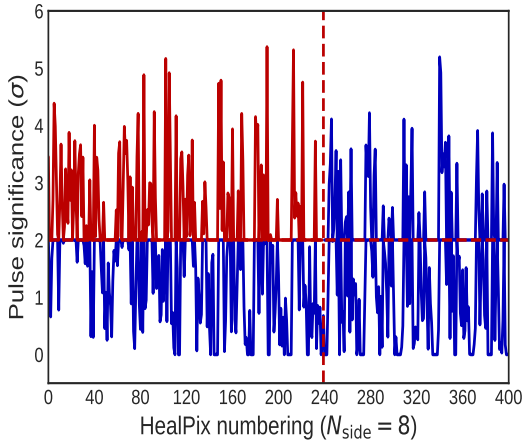


**Figure 4.** Pulse significance of different healpix bins. The horizontal red dashed line ( $2\sigma$ ) shows the applied cut on pulse significance, while the vertical one (239 HP number) shows the applied cut on HP bins which is introduced in Appendix B. 108 HP bins (red curves) after two cuts have been grouped into a subsample with a total exposure time of  $\sim 1710$  ks to the Crab pulsar, which are listed in Appendix D.

source coordinates that are defined in Figure 2. The  $\mathbf{E}_P$  is the electric vector of the source. The  $\mathbf{P}_N$  and the  $\mathbf{P}_E$  are the projection of the North and East vector of the J2000 coordinates respectively. The local definition of PA in source  $X'-Y'$  plane is  $PA_S$ , angle between  $\mathbf{E}_P$  and  $X'$ . While the formal PA definition in the J2000 North-East plane is  $PA_J$ , angle between  $\mathbf{E}_P$  and  $\mathbf{P}_N$  eastwards from the north. Hereby, we define the difference between the two value as rotation angle  $\phi_0$ .

Based on the POLAR zenith pointing data, the value of  $\phi_0$  for each arriving photon is calculated. We accumulate the data and bin  $\phi_0$  from  $0-180^\circ$  with a step size of  $3^\circ$ . The resulted exposure time of the Crab pulsar as a function of HP and  $\phi_0$  are shown in Figure 6, where one could clearly see a parabolic exposure time distribution. This variation of  $\phi_0$  suggests that we cannot simply accumulate the two-hit into modulation curves for each HP, since the  $\phi_0$  variation will counteract the modulation. We introduce a de-rotation method to align all  $\phi_0$  bins to zero. In this case, the modulation curves of

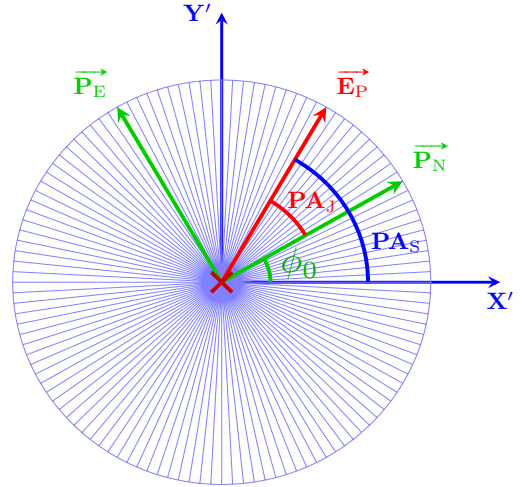


**Figure 5.** Two PA definitions and the rotation of the source. The view angle is from the source to POLAR. The  $X'-Y'$  plane is that of the source coordinates. The  $\mathbf{P}_N$ - $\mathbf{P}_E$  and  $\mathbf{E}_P$  are also shown here. The local definition of PA in the source  $X'-Y'$  plane is  $PA_S$ , angle between  $\mathbf{E}_P$  and  $X'$ . While the formal PA definition in the J2000 North-East plane is  $PA_J$ , the angle between  $\mathbf{E}_P$  and  $\mathbf{P}_N$  eastwards from the north. The difference between the two value is defined as the rotation angle  $\phi_0$ . The  $\phi_0$  space is binned from  $0-180^\circ$  with a step size of  $3^\circ$ .

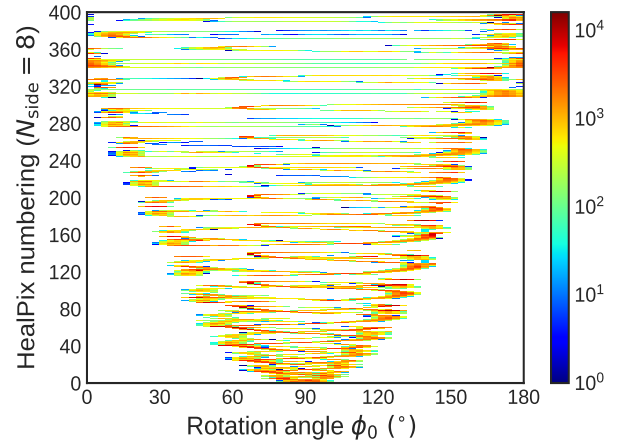


**Figure 6.** The exposure time of the Crab pulsar v.s. healpix bin and  $\phi_0$ . The Z-axis contains the exposure time of the Crab pulsar in unit of second. The exposure time has a parabolic distribution.

all  $\phi_0$  bins can be stacked, and there will be no difference between  $PA_J$  and  $PA_S$ . In Appendix A we show the de-rotation method, and check the validity of this method for polarization reconstruction. In Appendix B, we examine the systematic effect of the polarization reconstruction versus rotation angle  $\phi_0$  and incident angle  $\theta$ . Thereafter, based on the remaining HP subsample and the de-rotation method, we generate  $108 \times 3$  modulation curves for 108 HP and 3 phase intervals.

### 3 METHODOLOGY

Below in Section 3.1, we will describe the conventional polarization analysis method as a general introduction to gamma-ray polarimetry.

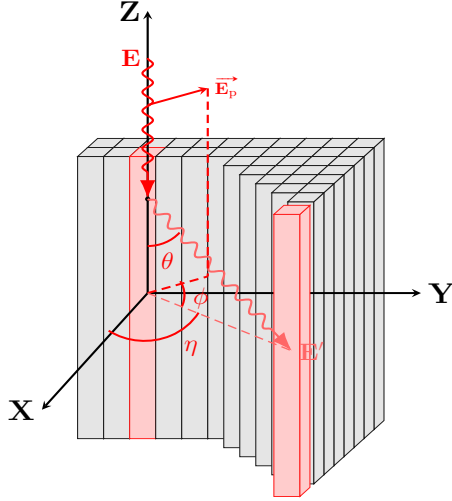


**Figure 7. Illustration of the Compton scattering process in a polarimeter.** The incident photon with an energy  $E$  Compton-scatters in one detector segment before moving towards a second detector segment with energy  $E'$ , where it interacts a second time. The polar scattering angle  $\theta$  is shown together with the azimuthal scattering angle  $\eta$ , both of which are measured in the detector. Angle  $\phi$ , which is defined as the angle between the intrinsic polarization vector and the momentum vector in the X-Y plane after Compton scattering, is preferentially  $90^\circ$  and suppressed at  $0^\circ$ .

We only use this method in Appendix A and Appendix B for a quick check on the PA and PD values. However, we did not use this method for the final polarization analysis in Zhang et al. (2019a) and neither in this paper; the methods used in the latter two works are presented in Section 3.2 and 3.3.

### 3.1 Conventional polarization reconstruction

The Compton scattering process of photons and free electrons follows the Klein-Nishina differential cross-section equation (Klein & Nishina 1929):

$$\frac{d\sigma_C}{d\Omega} = \frac{r_e^2}{2} \varepsilon^2 \left\{ \varepsilon + \varepsilon^{-1} - \sin^2 \theta + \sin^2 \theta \cos \left[ 2 \left( \eta + \frac{\pi}{2} \right) \right] \right\}, \quad (1)$$

where  $r_e$  is the classical electron radius;  $\varepsilon$  is the energy ratio of the outgoing photon over the energy of the incident photon, that is,  $E'/E$ ;  $\theta$  is the angle between the photon's incident and outgoing direction;  $\eta$  is defined as the azimuthal angle on the X-Y plane perpendicular to photon incident directions. Here we take the incidence direction to be along the detector's zenith as an example to discuss the polarization reconstruction. For a small off-axis angle, the situation is similar, however for a large off-axis angle there are additional effects which are discussed in section Appendix B. The scattering process is illustrated in Figure 7.

By integrating equation (1) over the solid angle, we have:

$$\sigma_C = 2\pi \int_0^\pi \frac{d\sigma_C}{d\Omega} \sin \theta d\theta. \quad (2)$$

For a photon with an initial energy  $E$  and PA of  $\Phi$  will, after scattering with free electrons, have a probability distribution for the azimuthal angle of the outgoing  $\eta$ :

$$P(\eta, E, \Phi) = \left\{ a(E) \times \cos \left[ 2 \left( \eta - \Phi + \frac{\pi}{2} \right) \right] + b(E) \right\} \times c(E), \quad (3)$$

where  $a(E)$ ,  $b(E)$  and  $c(E)$  are constants related to energy, and  $c(E)$  is the probability normalization factor. Assuming that a beam of photons is polarized, with a specific PD and PA,  $\eta$  of the outgoing photons should follow the trigonometrical probability function with the same phase. So the final scattering angle distribution (often called the modulation curve) accumulated over events, that is, the histogram of  $\eta$ , should have the equivalent form of equation (3), written as:

$$C(\eta, \Phi) = A \times \cos \left[ 2 \left( \eta - \Phi + \frac{\pi}{2} \right) \right] + B. \quad (4)$$

In case the beam is unpolarized, photons have different PA values, which result in different phases of  $\eta$ 's trigonometrical probability function that will cancel out the total modulation, so we expect the modulation curve to be flat.

By fitting the modulation curve with equation (4), we can obtain the relevant parameter values, where PA ( $=\Phi$ ) can be directly obtained by fitting. As for PD, we define the modulation factor:

$$\mu = \frac{A}{B} = \frac{C_{\max} - C_{\min}}{C_{\max} + C_{\min}}. \quad (5)$$

The modulation factor  $\mu$  can be obtained by fitting the measured modulation curve with equation (5). The modulation factor  $\mu$  reflects the PD of linear polarization of the photons. Generally, a polarimeter can be calibrated with a 100% linearly polarized source and verified by Monte Carlo simulation to obtain  $\mu_{100}$ . Then the PD of a measurement can be calculated by:

$$\text{PD} = \frac{\mu}{\mu_{100}}. \quad (6)$$

The above steps are for ideal conditions. In practice, a detector has geometric effects that may contaminate the modulation curve. It is therefore necessary to correct for these effects before fitting the modulation curve. While integrating equation (1), the geometric effect  $G(\eta, \theta_\gamma)$  needs to be taken into account, where  $\theta_\gamma$  is the incident angle of the source with respect to the detector. So for a polarized (PD =  $\Pi$ ) beam:

$$C_\Pi(\eta, \Phi, \theta_\gamma) = G(\eta, \theta_\gamma) \cdot 2\pi \int_0^\pi \frac{d\sigma_C^\Pi}{d\Omega} \sin \theta d\theta. \quad (7)$$

Correspondingly, for an unpolarized (PD = 0) beam (usually obtained by Monte Carlo simulation):

$$C_0(\eta, \Phi, \theta_\gamma) = G(\eta, \theta_\gamma) \cdot 2\pi \int_0^\pi \frac{d\sigma_C^0}{d\Omega} \sin \theta d\theta. \quad (8)$$

Therefore, the geometric effect can be eliminated by the following correction to obtain a geometric-corrected modulation curve:

$$C(\eta, \Phi, \theta_\gamma) = \frac{C_\Pi(\eta, \Phi, \theta_\gamma)}{C_0(\eta, \Phi, \theta_\gamma)} \cdot C_{\text{norm}}, \quad (9)$$

where  $C_{\text{norm}}$  is a normalization factor. Both measured and simulated modulation curves can be modified in this way for geometric effect correction. After that, by fitting  $C(\eta, \Phi, \theta_\gamma)$  with equation (4), and then calculate according to the equation (5) and (6), PD and PA can be reconstructed. The parameter errors can be acquired by fitting the measured and simulated modulation curves and carefully handling their error propagation.

### 3.2 POLAR GRB polarization reconstruction

The first polarization results of a subsample of 5 GRBs detected by POLAR were published in Zhang et al. (2019a). The analysis workflow presented there is different from (but equivalent to) the one described in Section 3.1. The differences are: 1) the geometric effect of a measured modulation curve will not be corrected with equation (9) since the Monte Carlo simulations include the same geometric effects; 2) the PA & PD are directly reconstructed by fitting measured modulation curves against a range of simulated modulation curves with different PD and PA. Subsequently, PD and PA are found using the least  $\chi^2$  method. Furthermore, Zhang et al. (2019a) has introduced a Bayesian approach for PA and PD reconstruction. The whole workflow is shown in Figure 8. Hereby we briefly introduce the analysis workflow:

- **Observation:** the GRB source interval and background intervals before and after the GRB are carefully defined. Then two-hit events are selected based on Li et al. (2018) and the scattering angles for these events are calculated to build modulation curves. The BKG (background) modulation curve is scaled with equivalent live time of the GRB interval, and the BKG modulation curve is subtracted from the SRC (source) modulation curve;

- **Simulation:** the MC software (Kole et al. 2017) is initially used to perform a set of 61 simulations (PD 100% and PA 0:3:180° (0 to 180° with step size of 3°); PD 0% and PA 0°) for the GRB using an energy spectrum and localization provided by other instruments. The 61 simulated data are processed using the same analysis pipeline used for the measurement data which could be referred to (Li et al. 2018);

- $\mathbf{B}_i$ : simulated modulation curves for different  $PD_i$  and  $PA_i$  (101×61 sets in total, PD: 0:1:100%, PA: 0:3:180°) are derived from the initial simulation set described above, by mixing those of the unpolarized flux and the 100% polarized flux ( $PA_i$ ) with the corresponding weights of (100%- $PD_i$ ) and  $PD_i$  respectively;

- $\Delta\chi^2$ : by fitting directly the measured (BKG subtracted) modulation curve with all the 6161 simulated ones the  $\chi^2$  values of the 6161 fits is retrieved. These are used to produce a  $\Delta\chi^2$  distribution in PD and PA space. Finally, the best fitted value  $\mathbf{A}$  ( $P\hat{D}$ ,  $P\hat{A}$ ) together with 1-2-3 sigma confidence intervals are deduced from  $\Delta\chi^2$  distribution;

- $\mathbf{B}'_i$ : we sample the modulation curves with a known PD and PA from  $\mathbf{B}_i$ , using the statistical quantity of the measured SRC modulation curves;

- $\mathbf{B}''_i$ : we introduce the BKG statistical fluctuations to  $\mathbf{B}'_i$  by adding and subtracting of sampled BKG modulation curves (each with the number of counts from the data), thus we obtain 'the measurement simulations' with known polarization parameters;

- $P(\mathbf{A}' | \mathbf{B}_i)$ : by fitting the  $\mathbf{B}''_i$  equal as described before in the  $\Delta\chi^2$  process, a best fitted value  $\mathbf{A}'$  ( $P\hat{D}$ ,  $P\hat{A}$ ) for a given  $\mathbf{B}_i$  will be recorded; this process is repeated for a statistically reasonable times (eg. 10000) to obtain a distribution of  $\mathbf{A}$ . After normalizing this distribution to 1, we have the conditional probability  $P(\mathbf{A}' | \mathbf{B}_i)$ , which indicates how likely  $\mathbf{A}$  will be measured with a given  $\mathbf{B}_i$ ;

- $P(\mathbf{B}_i | \mathbf{A})$ : with respect to the best fitted value  $\mathbf{A}$  ( $P\hat{D}$ ,  $P\hat{A}$ ) from  $\Delta\chi^2$  approach, we calculate the posterior distribution by assuming a prior distribution which is uniformly distributed within physical polarization space (PD 0-100% & PA 0-180°) and vanishes out of this space.

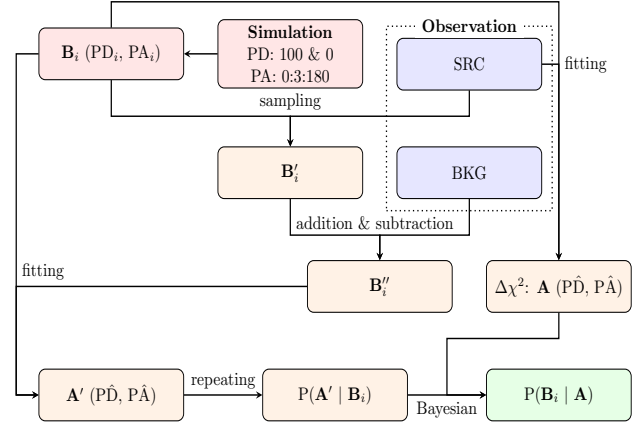


**Figure 8. Polarization Bayesian analysis workflow for GRB analysis.** This workflow is summarized from Zhang et al. (2019a). Finally the posterior written as  $P(\mathbf{B}_i | \mathbf{A})$  on the bottom right is generated for polarization reconstruction.

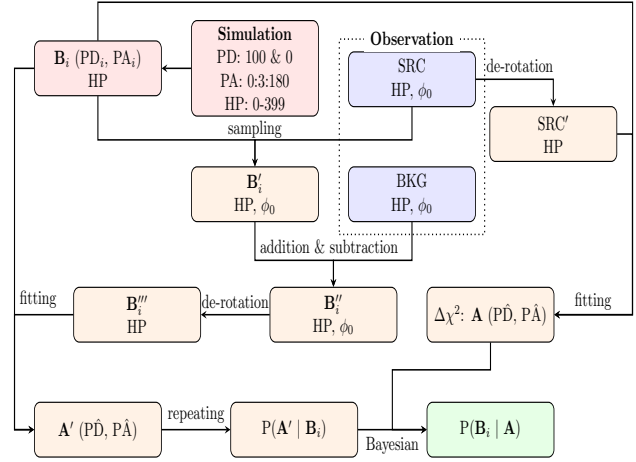


**Figure 9. Polarization Bayesian analysis workflow for the Crab analysis.** We adapted the GRB workflow to the Crab workflow with taking into account two more observational parameters which are the incident angle (reconstructed to healpix (HP) bin) and the rotation angle ( $\phi_0$ ). The  $\phi_0$  is corrected for using the de-rotation process, and then observation datasets in different HP bins are joint-fitted with simulation ones.

### 3.3 POLAR Crab polarization reconstruction

The Crab observations have two more observational parameters compared to the GRB analysis. These are the incident angle (HP) and the rotation angle ( $\phi_0$ ). So we adapt the GRB workflow to the Crab workflow as follows (only differences are shown, other parts are similar to the GRB workflow) which is also shown in Figure 9:

- **Observation:** for each (HP,  $\phi_0$ ) dataset, there are three intervals defined as AP (0.0-1.0), P1 (0.0-0.2 || 0.8-1.0) and P2 (0.2-0.6). The background interval is defined as the 0.6-0.8 phase range. The BKG modulation curves are scaled with equivalent phase length to the different on-pulse intervals, and the BKG modulation curve is subtracted from the SRC modulation curve. Note that the BKG contains the nebula and background, so there will be no nebula contribution in the remaining SRC curve;

- **Simulation:** a set of 61×400 (PD 100% and PA 0:3:180°; PD

0% and PA 0°; HP: 0-399) will be performed by using the spectrum of all phase intervals from Kuiper et al. (2001), we have added a 4% relative error to each bin in the simulated modulation curves in order to take into account the systematic uncertainties likely caused by spectral impact, similar to how this was done in Zhang et al. (2019a). As for  $\phi_0$ 's parameter space, it can be derived by shifting the curve using the  $\phi_0$  values in PA space;

- De-rotation: before fitting the measured modulation curves with simulated ones, we have to firstly accomplish a de-rotation process in order to fix  $\phi_0$  which can be found in detail from Appendix A. Note that, during this process, both the SRC and BKG modulation curves need to be corrected for geometric effect using the unpolarized simulated modulation curve of this dataset in order to allow for the de-rotation process to work;

- SRC': the de-rotation process is applied from SRC to SRC', then  $\phi_0$  parameter is fixed, and for each HP there will be only one modulation curve;

- $\mathbf{B}_i''$ : from  $\mathbf{B}_i''$  to  $\mathbf{B}_i'''$  is same as from SRC to SRC';

- $\Delta\chi^2$ : the fitting will be jointly among different HP bins, and a  $\Delta\chi^2$  distribution is obtained.

## 4 RESULTS AND DISCUSSION

Based on the methods described in the previous section, we obtain polarization measurements for the Crab pulsar. The posterior distributions are shown in Figure 10, Figure 11 and Figure 12 respectively. The best fitted values and the corresponding  $1\sigma$  deviations are AP (PD=14 $^{+15}_{-10}$ %, PA=108 $^{+33}_{-54}$ °), P1 (PD=17 $^{+18}_{-12}$ %, PA=174 $^{+39}_{-36}$ °) and P2 (PD=16 $^{+16}_{-11}$ %, PA=78 $^{+39}_{-30}$ °). From the cumulative probability of PD, we obtain the  $3\sigma$  upper limits on PD are AP (55%), P1 (66%) and P2 (57%) respectively, where the upper limits of P1 and P2 are more stringent than previous results and all of them reject a high PD scenario. Furthermore, the probability that the true PD is smaller than 1% for AP, P1 and P2 are 3.31%, 3.13% and 2.92% respectively, which, although not being a significant exclusion, suggest that the Crab pulsar emission is unlikely unpolarized. All the results of this work, together with previous work, are listed in Table D2.

We take PoGO+ as an example for detailed comparison. First of all, our results are in good agreement with each other within the margins of errors. Then, in order to have a direct impression, we plot the polarization vectors onto the Crab X-ray image taken with Chandra<sup>1</sup> in Figure 13. The black vectors in this plot are of POLAR, the red ones are for PoGO+. The cross point of these vectors is the Crab pulsar. Directions of the vectors are represented for the PA values counting from the top (North) to the left (East), and the lengths of the vectors are scaled by 33.5% (the dashed circle, PD of P2 by PoGO+) for PD values. For the polarization result of P1 by PoGO+, the marginalized posterior estimate (Marg.) is PD=0 $^{+29}_{-0}$ % and PA=153 ± 43°, but the maximum a posteriori probability estimate (MAP) gives PD=20.0±24.8% and PA=153 ± 36° (Chauvin et al. 2017). As a zero PD value (Marg. result) is unmeasurable (positive-definite) and makes also PA value meaningless, the MAP result (PD=20.0±24.8%, PA=153 ± 36°) is used in Figure 13 to demonstrate the polarization vector. The POLAR results of AP, P1 and P2 do not include the nebula contribution. The OP result of PoGO+ is contributed purely by the nebula, the PA of which is parallel to the spin axis of the Crab pulsar. The AP polarization results from PoGO+ contain also a nebula contribution which is more dominant

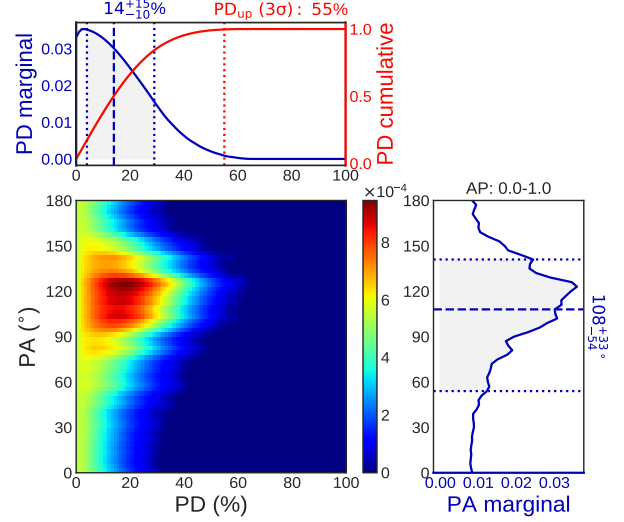


**Figure 10.** PD/PA posterior of AP phase interval. The best fitted values and the corresponding  $1\sigma$  deviations are PD=14 $^{+15}_{-10}$ %, PA=108 $^{+33}_{-54}$ °, the  $3\sigma$  upper limits on PD is 55%, and the probability that true PD is smaller than 1% is 3.31%.

than that of the pulsar, such that the fitted PA value is significantly different from that of POLAR. Due to the limited statistics, the phase intervals of P1 and P2 in POLAR are generally wider than those in PoGO+, which means that POLAR results include more components than that of PoGO+. The optical phase-resolved polarization results suggest that the PDs are higher in other phase ranges (especially in bridge and off-pulse) than those in the two narrow peaks, and the PAs swing through a large angle in both peaks. If the same polarization properties are similar at high energies, polarization result of a wider phase range should be different from that of a narrower one. This might explain the differences of PAs in P1 and P2 between POLAR and PoGO+. We should note here that as Figure 13 does not visualize the errors on PD and PA (can be found in Table D2), the attempt to interpret the differences between POLAR and PoGO+ applies only to the best fitted values without taking into account the margins of errors. In any case, the results on different definitions of phase intervals are difficult to compare, and we expect a finer phase-resolved polarization measurements with the same phase-intervals as those in optical bands will be achieved by future missions.

## 5 POLAR-2

POLAR-2 is a follow-up of the POLAR mission, which has been already selected to be launched to the China Space Station in around 2024 and will operate at least for two years (Kole 2019; Kole et al. 2021; Hulsman 2020; De Angelis et al. 2021). In order to improve the polarimetry precision, the POLAR-2 design takes two major improvements compared to POLAR, which are: 1) increasing the sensitive detector (scintillator array) modules from 25 to 100 (each module has 64 independent scintillator bars) so that the effective area will be approximately four times larger; 2) using a SiPM array (64 channels per module) together with its own front-end electronics (FEE) for readout which will lower the energy threshold of the detector pixel and increase the effective area at low energies. These features increase the SNR of a source detection significantly. Based on the preliminary design of POLAR-2, Monte-Carlo simulations have been performed to obtain the effective area as a function of

<sup>1</sup> <https://chandra.harvard.edu/photo/2009/crab/fits>

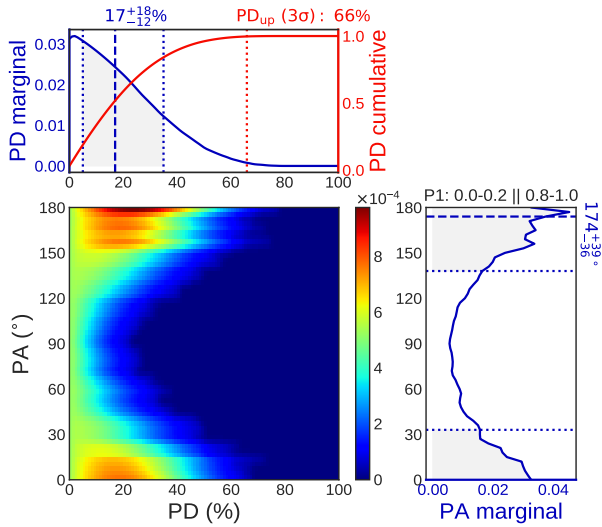


**Figure 11. PD/PA posterior of P1 phase interval.** The best fitted values and the corresponding  $1\sigma$  deviations are  $PD=17^{+18}_{-12}\%$ ,  $PA=174^{+39}_{-36}$ , the  $3\sigma$  upper limits on PD is 66%, and the probability that true PD is smaller than 1% is 3.13%.

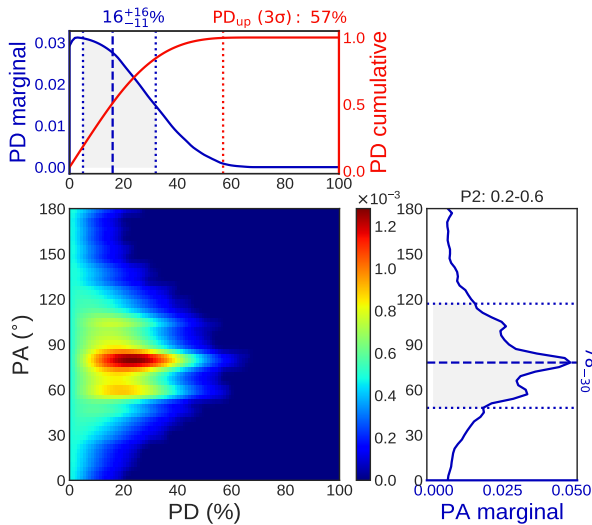


**Figure 12. PD/PA posterior of P2 phase interval.** The best fitted values and the corresponding  $1\sigma$  deviations are  $PD=16^{+16}_{-11}\%$ ,  $PA=78^{+39}_{-30}$ , the  $3\sigma$  upper limits on PD is 57%, and the probability that true PD is smaller than 1% is 2.92%.

energy. Based on Kole (2019) and Li et al. (2019), we consider the amount of measured photons with POLAR-2 is approximately 10 times that of POLAR in the 50-500 keV energy range by the convolution of the effective area and the Crab pulsar spectrum. Since the amount of background photons is expected to be directly proportional to the geometrical area of the instrument, we can conservatively assume the POLAR-2 background level to be 4 times that of POLAR. Detailed background simulations are however required in the future to provide a more accurate number for this.

Based on POLAR’s polarization reconstruction workflow for Crab introduced in Section 3.3, we perform the simulated polarization reconstruction of 2 years observation of the Crab pulsar for given polarization values, which is then joint-fitted among  $\mathbf{B}_i$  ( $PD_i$ ,  $PA_i$ , HP) and  $\mathbf{B}_i'''$  (HP). For the AP phase interval of the Crab pulsar,

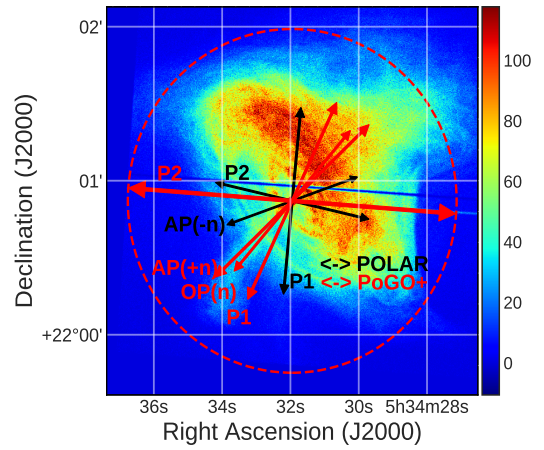


**Figure 13. Polarization vectors projected onto the Crab image taken by Chandra.** Directions of the vectors represent the PA values counting from the top (North) to the left (East). The lengths of the vectors are scaled according to the PD such that the longest one corresponds to 33.5% (the dashed circle, PD of P2 by PoGO+). The polarization vectors for AP, P1 and P2 as obtained from the POLAR analysis are shown in red while those of PoGO+ are, for comparison, shown in black. The AP from PoGO+ contains the nebula contribution (represented by the OP interval). The estimated  $20.0 \pm 24.8\%$  by maximizing a posterior probability is used for the PD of P1 by PoGO+. Note that this figure does not visualize the errors on PD and PA, which can be found in Table D2.

the  $\Delta\chi^2$  contour maps of given polarization values of ( $PD=0\%$ ,  $PA=0^\circ$ ), ( $PD=10\%$ ,  $PA=120^\circ$ ) and ( $PD=20\%$ ,  $PA=120^\circ$ ) are shown in Figure 14(a), 14(b) and 14(c) respectively. The contour lines from inner to outer are  $\chi^2$  (degree of freedom is 2) values of 2.3, 6.18, 11.83, 19.33 and 28.74, representing 1-5 sigma confidence levels respectively. Within 2 years of observation with POLAR-2, if the Crab pulsar is unpolarized, POLAR-2 will give 5 sigma upper limits on PD to a level of  $\sim 20\%$ . While if the Crab pulsar is 10% or 20% polarized, POLAR-2 will be able to confirm the Crab pulsar to be polarized with  $4\sigma$  or  $5\sigma$  confidence level.

## 6 SUMMARY

We present here the polarization measurement results of the AP, P1 and P2 phase intervals of the Crab pulsar performed using POLAR data. The measurements are in good agreement with previous results such as those from PoGO+. As POLAR can identify the pulsar, opposed to PoGO+ which can also investigate the nebula signal, it was capable of producing the most strict  $3\sigma$  PD upper limits of P1 (66%) and P2 (57%). All of these results reject a high PD scenario. Furthermore, the probability that the true PD is smaller than 1% for AP, P1 and P2 are 3.31%, 3.13% and 2.92% respectively, which, although not being a significant exclusion, show that the Crab pulsar emission is unlikely unpolarized. Although the polarization measurements of this work are lacking statistical precision, the polarimetry methodology developed here could be employed for other wide FoV polarimeters and thereby increases the scientific targets available to these instruments from transient sources to pulsars. Using the polarimetry methodology and Monte-Carlo simulations we extrapolate the polarization reconstruction ability of POLAR-2 with 2 years observation to the Crab pulsar. We can therefore conclude that with 2 years of observation to the Crab pulsar POLAR-2 will be able to confirm the emission to be polarized with  $5\sigma$  confidence level in case

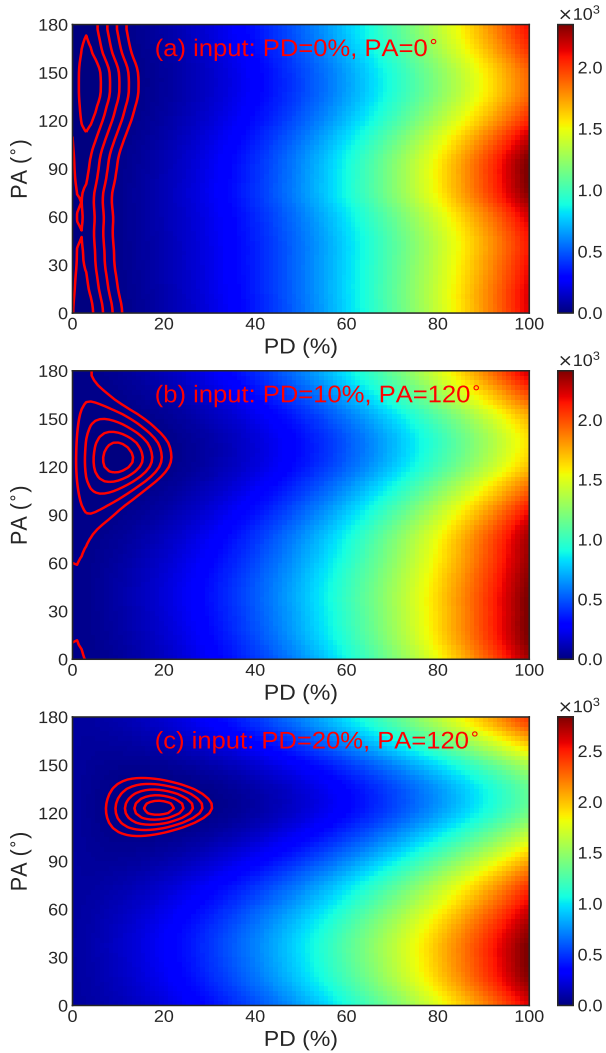


**Figure 14. Simulated POLAR-2 polarization reconstruction for the AP interval of the Crab pulsar with 2 years observation.** The  $\Delta\chi^2$  contour maps from top to bottom are for given polarization values of (PD=0%, PA=0°), (PD=10%, PA=120°) and (PD=20%, PA=120°) respectively. The contour lines from inner to outer are  $\chi^2$  (degree of freedom is 2) values of 2.3, 6.18, 11.83, 19.33 and 28.74, representing 1-5 sigma confidence levels respectively.

the polarization is 20%, while it can be done with  $4\sigma$  confidence level if it is polarized at 10%. In case the emission is unpolarized, POLAR-2 could obtain  $5\sigma$  upper limits at a level of  $\sim 20\%$ . With sufficient statistics of POLAR-2, a finer phase-resolved polarization measurements of the Crab pulsar can also be obtained. Additionally, as POLAR-2 will have an increased energy range, spanning from 30 keV to 800 keV, energy dependent polarization measurements will also be within the possibilities. Such measurements can be combined with those from photoelectron-track polarimeters onboard the IXPE mission (Soffitta et al. 2021) and the eXTP mission (Zhang et al. 2019b) in the near future. At the time of the launch of POLAR-2, IXPE is expected to have performed precise measurements of the Crab emission in the 2-10 keV energy range, while eXTP will likely increase the precision during, or after, the POLAR-2 mission.

## ACKNOWLEDGMENTS

We gratefully acknowledge the financial support from the National Natural Science Foundation of China (Grant No. 11961141013, 11503028), the Joint Research Fund in Astronomy under the cooperative agreement between the National Natural Science Foundation of China and the Chinese Academy of Sciences (Grant No. U1631242), the Strategic Priority Research Program of the Chinese Academy of Sciences (Grant No. XDB23040400), the National Natural Science Foundation of China (Grants U1838201, U1838202 and U1838104), the Youth Innovation Promotion Association of Chinese Academy of Sciences (Grant No. 2014009), the Xie Jialin Foundation of the Institute of High Energy Physics, Chinese Academy of Sciences (Grant No. 542019IHEPZZBS10210), the National Basic Research Program (973 Program) of China (Grant No. 2014CB845800), the Swiss Space Office of the State Secretariat for Education, Research and Innovation (ESA PRODEX Programme), and the National Science Center of Poland (Grant No. 2015/17/N/ST9/03556). H.C.L. acknowledge the support from the University of Chinese Academy of Sciences (UCAS) Joint PhD Training Program. M.K. and N.D.A. acknowledge the support of the Swiss National Science Foundation.

## DATA AVAILABILITY

The observation data used in this article were obtained from POLAR collaboration (<https://www.astro.unige.ch/polar/>). The high-level data product derived in this research could be shared upon reasonable request to the corresponding author.

## REFERENCES

- Burgess J. M., Kole M., Berlato F., Greiner J., Vianello G., Produit N., Li Z. H., Sun J. C., 2019, *A&A*, **627**, A105
- Chattopadhyay T., 2021, *Journal of Astrophysics and Astronomy*, **42**, 106
- Chauvin M., Roques J. P., Clark D. J., Jourdain E., 2013, *ApJ*, **769**, L37
- Chauvin M., et al., 2017, *Scientific Reports*, **7**, 7816
- Cheng K. S., Ho C., Ruderman M., 1986a, *ApJ*, **300**, 500
- Cheng K. S., Ho C., Ruderman M., 1986b, *ApJ*, **300**, 522
- De Angelis N., et al., 2021, arXiv e-prints, p. arXiv:2109.02978
- Dean A. J., et al., 2008, *Science*, **321**, 1183
- Du Y. J., Qiao G. J., Han J. L., Lee K. J., Xu R. X., 2010, *MNRAS*, **406**, 2671
- Feng H., et al., 2020, *Nature Astronomy*, **4**, 511
- Forot M., Laurent P., Grenier I. A., Gouiffès C., Lebrun F., 2008, *ApJ*, **688**, L29
- Górski K. M., Hivon E., Banday A. J., Wandelt B. D., Hansen F. K., Reinecke M., Bartelmann M., 2005, *ApJ*, **622**, 759
- Harding A. K., Kalapotharakos C., 2017, *ApJ*, **840**, 73
- Hirovani K., 2008, *ApJ*, **688**, L25
- Hitomi Collaboration et al., 2018, *PASJ*, **70**, 113
- Hulsman J., 2020, in Society of Photo-Optical Instrumentation Engineers (SPIE) Conference Series. p. 114442V (arXiv:2101.03084), doi:10.1117/12.2559374
- Jourdain E., Roques J. P., 2019, *ApJ*, **882**, L29
- Klein O., Nishina T., 1929, *Zeitschrift fur Physik*, **52**, 853
- Kole M., 2019, in 36th International Cosmic Ray Conference (ICRC2019). p. 572
- Kole, M. and Sun, J.C. 2022, Handbook of X-ray and Gamma-ray Astrophysics. Springer
- Kole M., et al., 2017, *Nuclear Instruments and Methods in Physics Research A*, **872**, 28
- Kole M., et al., 2020, *A&A*, **644**, A124
- Kole M., et al., 2021, arXiv e-prints, p. arXiv:2109.02977
- Kuiper L., Hermsen W., Cusumano G., Diehl R., Schönfelder V., Strong A., Bennett K., McConnell M. L., 2001, *A&A*, **378**, 918

- Li T. P., Ma Y. Q., 1983, *ApJ*, 272, 317
- Li H., POLAR Collaboration 2021, arXiv e-prints, p. arXiv:2109.03142
- Li H., Ge M., Wu B., Polar Collaboration 2017, in 35th International Cosmic Ray Conference (ICRC2017), p. 820
- Li Z., et al., 2018, *Nuclear Instruments and Methods in Physics Research A*, 900, 8
- Li H.-C., et al., 2019, *Journal of High Energy Astrophysics*, 24, 15
- Moran P., Shearer A., Mignani R. P., Słowikowska A., De Luca A., Gouiffès C., Laurent P., 2013, *MNRAS*, 433, 2564
- Pétri J., 2013, *MNRAS*, 434, 2636
- Produit N., et al., 2005, *Nuclear Instruments and Methods in Physics Research A*, 550, 616
- Produit N., et al., 2018, *Nuclear Instruments and Methods in Physics Research A*, 877, 259
- Ruderman M. A., Sutherland P. G., 1975, *ApJ*, 196, 51
- Słowikowska A., Kanbach G., Kramer M., Stefanescu A., 2009, *MNRAS*, 397, 103
- Soffitta P., et al., 2021, *AJ*, 162, 208
- Takata J., Chang H. K., Cheng K. S., 2007, *ApJ*, 656, 1044
- Vadawale S. V., et al., 2018, *Nature Astronomy*, 2, 50
- Weisskopf M. C., Cohen G. G., Kestenbaum H. L., Long K. S., Novick R., Wolff R. S., 1976, *ApJ*, 208, L125
- Weisskopf M. C., Silver E. H., Kestenbaum H. L., Long K. S., Novick R., 1978, *ApJ*, 220, L117
- Xiong S., Wang Y., Li Z., Sun J., Zhao Y., Li H., Huang Y., Polar Collaboration 2017, in 35th International Cosmic Ray Conference (ICRC2017), p. 640
- Zhang S.-N., et al., 2019a, *Nature Astronomy*, 3, 258
- Zhang S., et al., 2019b, *Science China Physics, Mechanics, and Astronomy*, 62, 29502
- Zheng S., et al., 2017, *Scientia Sinica Physica, Mechanica & Astronomica*, 47, 099505

## APPENDIX A: DE-ROTATION METHOD

In order to fix the  $\phi_0$  parameter defined in Figure 5, a de-rotation process needs to be implemented. Here we show a toy simulation that demonstrates this method. We take a certain incident angle of the source with respect to the detector zenith axis ( $\theta = 42.6^\circ$ ,  $\phi = 52.3^\circ$ ). Then, we assume the true PD is 100%, and the  $PA_J$  is  $0^\circ$ . By dividing  $\phi_0$  in bins from  $0 - 180^\circ$  with a size of  $3^\circ$ , we obtain 61 bins of  $\phi_0$ . For each  $\phi_0$  bin, the  $\phi_0$  value will be directly added into  $PA_J$ , which results in 61 bins of  $PA_S$ . The remaining steps are as follows:

- We simulate a sample of  $PD=100\%$  &  $PA_S = 0 : 3 : 180^\circ$  and  $PD=0\%$  &  $PA_S = 0^\circ$  (for geometric effect correction) with equal exposure time. Thereafter, we calculate the scattering angles and generate the modulation curves for the sample. The original modulation curves of 100% PD as a function of  $\phi_0$  can be seen in Figure A1(a), where the pattern is dominated by geometric effect and there is no sign of  $\phi_0$  dependence;

- Based on equation (9), we can use the unpolarized modulation curve to correct the geometric effect from Figure A1(a). Note here that the unpolarized curve is independent on  $\phi_0$ . The geometric-corrected pattern is shown in Figure A1(b). From this pattern, one can clearly see a linear correlation between the modulation curves and  $\phi_0$  bins. We further fit the modulation curves along  $\phi_0$  bins by using equation (4) and (5). The reconstructed  $\mu_{100}$  factor as a function of  $\phi_0$  can be found in Figure A1(d), there is small sinusoidal variation (this is more significant for large off-axis incidence which is investigated in Appendix B), but it can be fitted by  $\mu_{100} = 0.239$ . The reconstructed PA ( $PA_S$ ) as a function of  $\phi_0$  can be found in Figure A1(e), where the PA values are proportional to  $\phi_0$ ;

- By shifting the modulation curves with the corresponding  $\phi_0$  values, we obtain a perfectly aligned pattern which can be found in

Figure A1(c). In this pattern, all modulation curves are aligned to  $\phi_0 = 0^\circ$ , and thus the modulation curves can be stacked. We use the exposure time ratio as a weight to sum over  $\phi_0$  bins, the weighted sum of modulation curves is shown in Figure A1(f). By fitting it, we get  $\mu_{100} = 0.239 \pm 0.074$  which agrees with Figure A1(d), and  $PA = 0 \pm 9^\circ$  which agrees with assumption of  $PA_J = 0^\circ$ .

This toy simulation shows a way to de-rotate  $\phi_0$  (makes it fixed to be zero), which is to shift the modulation curves (after geometric effect correction) by the amount corresponding to the  $\phi_0$  values. Then the modulation curves can be added together with exposure time ratios as weight. More importantly, the fitting shows that the weighted sum will precisely retain the input polarization information unchanged, which allows us to apply the de-rotation process of  $\phi_0$  in our dataset and move forward to further polarization analysis.

## APPENDIX B: SYSTEMATIC EFFECT

In Appendix A, Figure A1(d) and (e), we see some hints of systematic effects. So before we apply the de-rotation method to our datasets, we further checked the validity of this method for several incident angles, and examined if there are significant systematic effects for the polarization reconstruction. We run a set of toy simulations equal to the one in Appendix A for different incident angles of  $\theta$  ( $10:10:90^\circ$ ).

The reconstructed  $\mu_{100}$  factor as a function of incident angle  $\theta$  and rotation angle  $\phi_0$  is shown in Figure B1. There are two pieces of information which can be retrieved from this plot: 1) the  $\mu_{100}$  factor rapidly decreases with  $\theta$  value; 2) the  $\mu_{100}$  factor reconstruction has more significant effects on top of the  $180^\circ$  modulation (additional sinusoidal systematic effect) when  $\theta$  increases, and when  $\theta > 70^\circ$  this additional effect becomes non-negligible. Based on Figure A1 (e), we further define the residual of PA reconstruction, which is  $PA - \phi_0$ . Figure B2 shows the residual as a function of incident angle  $\theta$  and rotation angle  $\phi_0$ . Likewise, we see a similar sinusoidal systematic effect for increasing  $\theta$ . A stable  $\mu_{100}$  factor and good linear PA &  $\phi_0$  correlation are crucial for the de-rotation process and polarization reconstruction. It should be noted here that the additional effects seen in the curve are understood and are a result of photons scattering off materials surrounding the detector. The kinematics of this scattering are dependent on the intrinsic polarization of the photons and therefore remain after correcting with the unpolarized modulation curve. The effect is described in more detail in (Kole, M. and Sun, J.C. 2022). In the work presented here, in order to prevent unwanted systematic effects from potentially entering the analysis we decided to get rid of data when  $\theta > 70^\circ$ .

## APPENDIX C: DIRECT FITTING RESULTS

The joint-fitting among simulated  $B_i$  ( $PD_i, PA_i$ ) and observed SRC' generates a  $\Delta\chi^2$  contour map which can be used to determine the best fitted value  $A_i$  ( $PD, PA$ ). The  $\Delta\chi^2$  contour maps of AP, P1 and P2 are shown in Figure C1 (a), (b) and (c) respectively. The contour lines in these plots from left to right are  $\chi^2$  (degree of freedom is 2) values of 2.3, 6.18, 11.83, 19.33 and 28.74, representing 1-5 sigma confidence levels respectively.

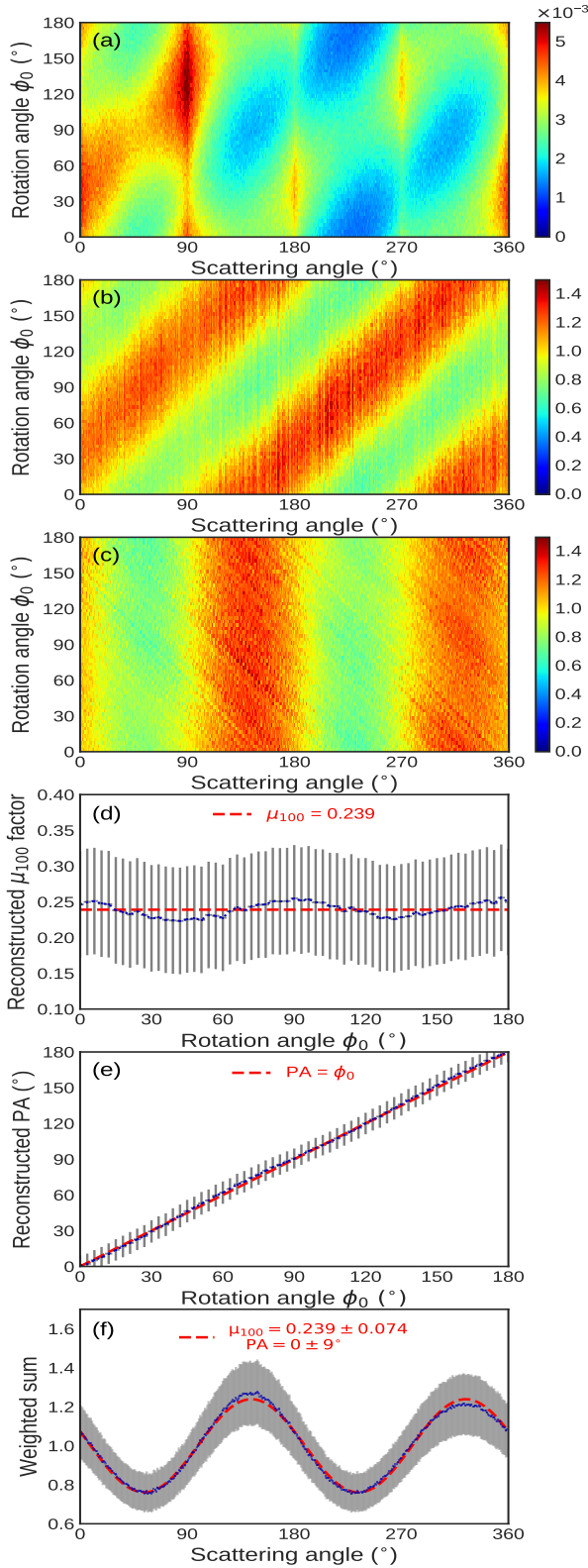


**Figure A1. The de-rotation method.** (a) is the original (simulated) pattern of the modulation curve v.s. rotation angle  $\phi_0$ ; (b) is the pattern of (a) after geometric-correction; (c) is the pattern after correcting for  $\phi_0$  (rotate modulation curves with the corresponding  $\phi_0$  values, then  $\phi_0 = 0^\circ$ ); (d) is the reconstructed  $\mu_{100}$  v.s.  $\phi_0$ ; (e) is the reconstructed PA v.s.  $\phi_0$ ; (f) is the weighted sum of (c) over  $\phi_0$  with exposure time as weight.

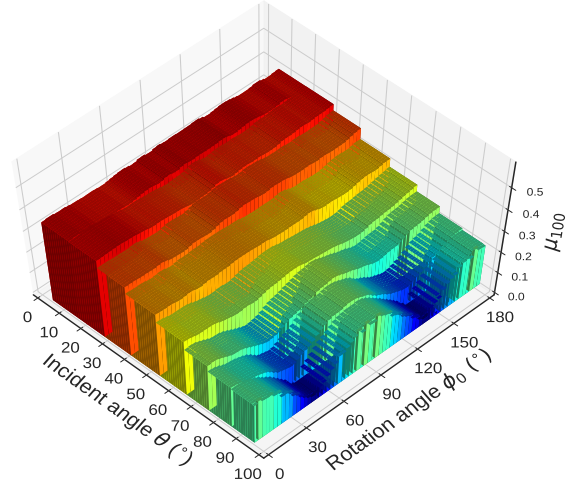


**Figure B1. The reconstructed  $\mu_{100}$  v.s. rotation angle  $\phi_0$  and incident angle  $\theta$ .** The  $\mu_{100}$  factor can be seen to rapidly decrease with  $\theta$  value increases especially at some specific  $\phi_0$  angles. Additionally, it can be observed to have significant harmonics (additional sinusoidal systematic effect) when  $\theta$  is larger.

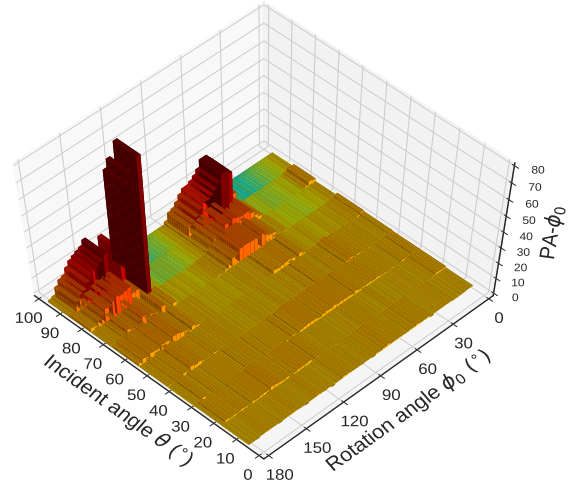


**Figure B2. The reconstructed PA minus  $\phi_0$  v.s. rotation angle  $\phi_0$  and incident angle  $\theta$ .** The PA has non-negligible effects (additional sinusoidal systematic effect) when  $\theta$  is larger than  $70^\circ$ .

#### APPENDIX D: TABLES

Here listed two tables including the observation subsample (Table D1) defined by Section 2 and polarization results (Table D2) obtained from this work and the previous works that introduced in Section 1.

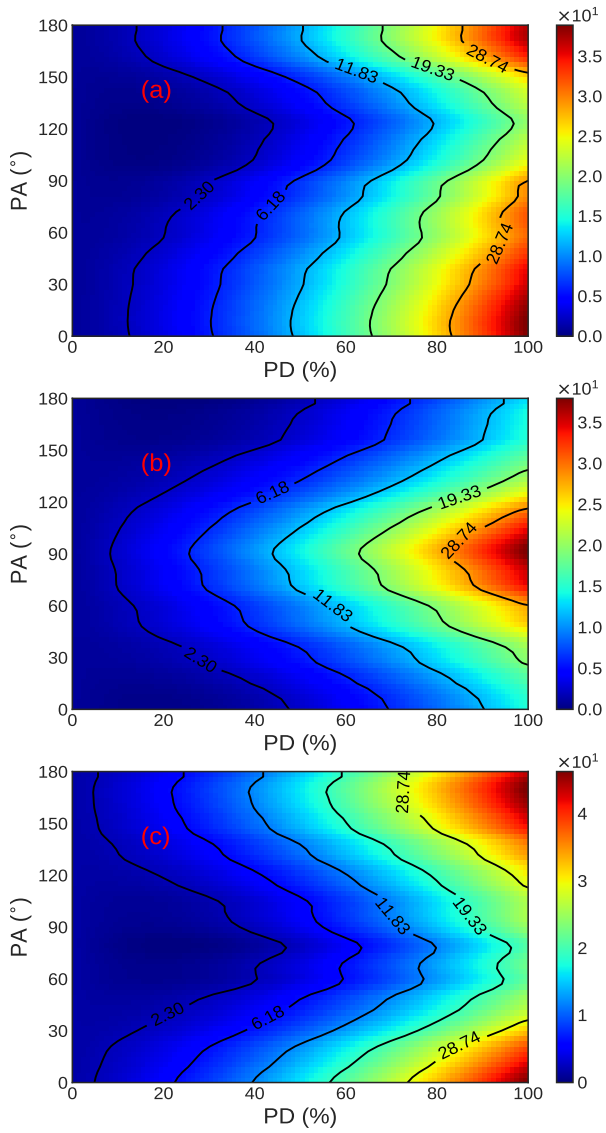


**Figure C1. The PD/PA  $\Delta\chi^2$  contour maps.** Panel (a), (b) and (c) are of the AP, P1 and P2 phase interval respectively. The contour lines in these plots from left to right are  $\chi^2$  (degree of freedom is 2) values of 2.3, 6.18, 11.83, 19.33 and 28.74, representing 1-5 sigma confidence levels respectively.

**Table D1. Subsample of the Crab pulsar observations for polarization analysis.** It is sorted by pulse significance in descending order, and contains 108 HP bins and ~1710 ks exposure times in total.

HP No.	$\theta$ (°)	$\phi$ (°)	significance ( $\sigma$ )	exposure time (s)	HP No.	$\theta$ (°)	$\phi$ (°)	significance ( $\sigma$ )	exposure time (s)
190	60.00	163.13	5.37	23030	88	41.86	57.86	2.99	13640
213	65.38	56.25	5.32	22109	89	41.86	70.71	2.98	14883
102	41.86	237.86	5.16	9090	117	48.19	61.88	2.92	14919
105	41.86	276.43	4.92	50118	73	35.66	202.50	2.92	8284
83	35.66	352.50	4.88	26669	65	35.66	82.50	2.92	8041
150	54.31	67.50	4.79	19040	165	54.31	236.25	2.85	8155
221	65.38	146.25	4.75	12177	215	65.38	78.75	2.82	11400
148	54.31	45.00	4.73	24194	156	54.31	135.00	2.82	9319
5	11.72	67.50	4.38	12591	157	54.31	146.25	2.74	9928
92	41.86	109.29	4.24	32009	93	41.86	122.14	2.74	12605
78	35.66	277.50	4.21	36787	184	60.00	95.63	2.73	16470
168	54.31	270.00	4.20	27964	24	23.56	11.25	2.71	17758
111	41.86	353.57	4.16	23033	119	48.19	84.38	2.71	11207
180	60.00	50.63	4.15	17433	199	60.00	264.38	2.70	18473
182	60.00	73.13	4.01	17415	4	11.72	22.50	2.70	16194
40	29.57	9.00	4.00	23905	19	17.61	225.00	2.70	9850
6	11.72	112.50	3.99	10384	10	11.72	292.50	2.69	12292
66	35.66	97.50	3.98	10954	134	48.19	253.13	2.67	20281
160	54.31	180.00	3.94	11043	12	17.61	15.00	2.67	16109
18	17.61	195.00	3.87	9885	48	29.57	153.00	2.65	9711
181	60.00	61.88	3.79	19086	127	48.19	174.38	2.65	7039
125	48.19	151.88	3.74	17653	217	65.38	101.25	2.64	18412
68	35.66	127.50	3.73	9752	22	17.61	315.00	2.58	16647
23	17.61	345.00	3.73	15819	219	65.38	123.75	2.58	6078
232	65.38	270.00	3.72	25103	137	48.19	286.88	2.57	41851
62	35.66	37.50	3.71	13127	16	17.61	135.00	2.56	9402
11	11.72	337.50	3.67	15539	149	54.31	56.25	2.56	18399
28	23.56	101.25	3.66	9133	86	41.86	32.14	2.52	19243
212	65.38	45.00	3.63	26595	59	29.57	351.00	2.52	28498
116	48.19	50.63	3.53	15189	216	65.38	90.00	2.42	11091
106	41.86	289.29	3.53	30453	29	23.56	123.75	2.41	8225
67	35.66	112.50	3.52	10780	214	65.38	67.50	2.39	18448
61	35.66	22.50	3.51	21940	44	29.57	81.00	2.36	8741
27	23.56	78.75	3.50	10359	90	41.86	83.57	2.33	11715
122	48.19	118.13	3.48	22075	124	48.19	140.63	2.32	13179
77	35.66	262.50	3.46	23034	17	17.61	165.00	2.30	9994
0	5.85	45.00	3.45	11652	87	41.86	45.00	2.27	13121
30	23.56	146.25	3.44	7739	33	23.56	213.75	2.25	8592
42	29.57	45.00	3.44	14567	14	17.61	75.00	2.23	11740
115	48.19	39.38	3.42	21977	151	54.31	78.75	2.17	12437
169	54.31	281.25	3.40	17353	104	41.86	263.57	2.16	25649
152	54.31	90.00	3.36	11146	81	35.66	322.50	2.14	13400
185	60.00	106.88	3.31	18461	135	48.19	264.38	2.11	21682
15	17.61	105.00	3.24	9896	8	11.72	202.50	2.10	11479
20	17.61	255.00	3.22	9674	193	60.00	196.88	2.09	3006
43	29.57	63.00	3.22	13808	123	48.19	129.38	2.08	11249
26	23.56	56.25	3.16	15508	63	35.66	52.50	2.07	13838
187	60.00	129.38	3.13	6616	41	29.57	27.00	2.06	14790
121	48.19	106.88	3.13	20974	120	48.19	95.63	2.06	15626
71	35.66	172.50	3.10	6685	158	54.31	157.50	2.04	23707
69	35.66	142.50	3.06	10878	166	54.31	247.50	2.03	8921
7	11.72	157.50	3.05	11112	21	17.61	285.00	2.02	12400
36	23.56	281.25	3.05	12717	161	54.31	191.25	2.01	10340
136	48.19	275.63	3.01	33379	189	60.00	151.88	2.01	12645

**Table D2. Polarization measurements of the Crab pulsar & nebula by POLAR and other instruments**

Mission	Publication	Energy band (keV)	Exposure time (ks)	Phase range	PA (°)	PD (%)	PD <sub>down</sub> <sup>%</sup> (confidence%)	PD <sub>up</sub> <sup>%</sup> (confidence%)
POLAR	this work	50–500	~1710	AP (-n)	$108^{+33}_{-54}$	$14^{+15}_{-10}$	N/A	55 (99.7)
				P1	$174^{+39}_{-36}$	$17^{+18}_{-12}$		66 (99.7)
				P2	$78^{+39}_{-30}$	$16^{+16}_{-11}$		57 (99.7)
PolarLight	Feng et al. (2020)	3.0–4.5	~660	AP (+n)	$145.8 \pm 5.7$	$15.3^{+3.1}_{-3.0}$	N/A	N/A
				P1+P2	$147.6 \pm 7.0$	$15.8 \pm 3.9$		
				OP	$142.4 \pm 11.0$	$14.0^{+5.2}_{-5.4}$		
Hitomi SGD	Hitomi Collaboration et al. (2018)	60–160	5	AP (+n)	$110.7^{+13.2}_{-13.0}$	$22.1 \pm 10.6$	N/A	N/A
Astrosat CZTI	Vadawale et al. (2018)	100–380	800	AP (+n)	$143.5 \pm 2.8$	$32.7 \pm 5.8$	N/A	N/A
				OP	$140.9 \pm 3.7$	$39.0 \pm 10.0$		
PoGO+	Chauvin et al. (2017)	20–160	92	AP (+n)	$131.3 \pm 6.8$	$20.9 \pm 5.0$	N/A	32.5(99)
				P1	$153 \pm 43$	$0^{+29}_{-0}$ (20.0±24.8)		72.6 (99)
				P2	$86 \pm 18$	$33.5^{+18.6}_{-22.3}$		80.9 (99)
				OP	$137 \pm 15$	$17.4^{+8.6}_{-9.3}$		37.3 (99)
INTEGRAL SPI	Jourdain & Roques (2019)	130–400	~6400	AP (+n)	$120 \pm 6$	$24 \pm 4$	N/A	N/A
	Chauvin et al. (2013)	130–400	600	AP (+n)	$117 \pm 9$	$28 \pm 6$		
	Dean et al. (2008)	100–1000	N/A	OP	$123 \pm 11$	$47 \pm 10$		
INTEGRAL IBIS	Forot et al. (2008)	200–800	1200	AP (+n)	$100 \pm 11$	$47^{+19}_{-13}$	N/A	N/A
				P1+P2	$70 \pm 20$	$42^{+30}_{-16}$		
				OP	$120.6 \pm 8.5$	N/A		
OSO	Weisskopf et al. (1978)	2.6	~256	OP	$156.4 \pm 1.4$	$19.2 \pm 1.0$	N/A	N/A
		5.2			$152.6 \pm 4.0$	$19.5 \pm 2.8$		
	Weisskopf et al. (1976)	2.6	N/A	AP (+n)	$161.1 \pm 2.8$	$15.7 \pm 1.5$		
		5.2			$155.5 \pm 6.6$	$18.3 \pm 4.2$		

Notes:

1.  $^{+\uparrow}$  or  $^{\downarrow}$ : one sigma up(+)/down(-) deviation;
2. PD<sub>down</sub> (99%) & PD<sub>up</sub> (99%): upper and lower limit for PD with 99% confident level respectively;
3. ±n: the Crab nebula was(+) included in Averaged-Phase (AP) or not(-);
4. OP: off pulse, represent for the Crab nebula;
5. N/A: not been shown from the publication;
6. The PD of P1 by PoGO+ is  $0^{+29}_{-0}$ % with the marginalized estimate and 20.0±24.8% (shown in Figure 13) with the maximum a posterior probability estimate.